Long baseline navigation filter with clock offset estimation

Tiago Silva and Pedro Batista

Nonlinear Dynamics, vol. 100, pp. 2557-2573, May 2020

https://doi.org/10.1007/s11071-020-05636-0

Cite as: Tiago Silva and Pedro Batista, "Long baseline navigation filter with clock offset estimation," Nonlinear Dynamics, vol. 100, pp. 2557-2573, May 2020. DOI: 10.1007/s11071-020-05636-0

Nonlinear Dyn manuscript No.
(will be inserted by the editor)

Long Baseline Navigation Filter with Clock Offset Estimation

Tiago Silva · Pedro Batista

Received: April 4, 2020

Abstract In underwater navigation, the global positioning system is unavailable, hence other solutions must be pursued in the development of navigation systems. In this paper, filters for the position, linear velocity, and acceleration of underwater vehicles are derived by combining a long baseline acoustic positioning system with an inertial navigation system. A dynamic model is devised via state augmentation, including the bias of the pseudo-ranges, which accounts for the effect of the unknown offset between the emitters' and receivers' clocks. With this technique, the resulting dynamics are linear, in spite of the original nonlinear nature of the problem. The proposed solution, which includes the explicit dynamic estimation of the bias of the pseudo-ranges, is a linear Kalman filter. The observability of the system is assessed, which allows to establish globally exponentially stable error dynamics. The performance of the solution is evaluated with realistic simulation results, considering sensor noise and discrete-time measurements. Finally, the comparison with the extended Kalman filter, the unscented Kalman filter, and the Bayesian Cramér-Rao bound is presented, including Monte Carlo simulations. This comparison shows the goodness of the proposed solution, which converges for all initial conditions and exhibits performance comparable to the EKF and the UKF, whereas the EKF and UKF are shown to lack global convergence.

Keywords underwater navigation systems · long baseline · clock synchronization · pseudo-range

Corresponding author: Pedro Batista.
Funding: This work was partially supported by the LARSyS - FCT Plurianual funding 2020-2023 and through the FCT project DECENTER [LISBOA-01-0145-FEDER-029605], funded by the Programa Operacional Regional de Lisboa 2020 and PIDDAC programs.
The authors are with the Institute for Systems and Robotics, Laboratory for Robotics and Engineering Systems, Portugal. The authors are also with Instituto Superior Técnico, Universidade de Lisboa, Portugal. {tiago.filipe.silva@tecnico.ulisboa.pt, pbatista@isr.tecnico.ulisboa.pt}

1 Introduction

Accurate navigation systems are essential for the successful operation of autonomous and non-autonomous vehicles, providing navigation data that is useful, whether for geo-referencing, guidance, or for control purposes. Most navigation systems contain an inertial navigation system (INS), which uses data obtained from the sensors of an Inertial Measurement Unit (IMU). While the INS is self-contained, and offers good performance for short missions, it suffers from problems with open-loop integration of both the sensors' noise and bias. Over time, the open-loop integration increases the errors of states of interest, such as the heading and position of the vehicle, as evidenced in [30]. Circumventing these problems involves implementing sensor fusion, i.e., coupling the instruments of an INS, such as an IMU and Attitude and Heading Reference System (AHRS), with additional sensors, which allows the design of observers or filters that correct the estimation error via feedback.

A typical additional sensor used to complement an IMU and AHRS is a satellite-based navigation device such as the global positioning system (GPS), with examples of aided navigation seen in, e.g., [3], [9], [19], [5], and [26]. Underwater navigation systems are of great importance, being used by divers, unmanned underwater vehicles (UUV) such as autonomous underwater vehicles (AUV), and remotely operated underwater vehicles (ROV). However, the attenuation that the electromagnetic field suffers underwater renders the GPS

useless. For this reason, to design a navigation system that works in this environment, other devices must be considered. Unlike GPS signals and most radio signals, acoustic waves are not quickly absorbed, and propagate far underwater and at a measurable rate. This enables the measurement of the distance between a receiver and one or a series of transponders, as seen in [18]. Acoustic navigation systems are generally categorized into three broad classes: Long Baseline (LBL), Ultra Short Baseline (USBL), and Short Baseline (SBL). As a rule of thumb, the orders of magnitude [21] are displayed in Table 1.

Table 1: Orders of magnitude of the baseline for the LBL, SBL, and USBL

Baseline	**Order of magnitude**
LBL	100m to 6000m
SBL	20m to 50m
USBL	less than 10cm

While harder to install, LBL systems have the highest accuracy among the acoustic positioning methods. The baseline transponders are installed in the work reference site, and the geometry of the baseline transponders' network is favorable for position estimation. Furthermore, it operates fully underwater, which proves to be convenient in situations where the sea surface is far from the work site. A GPS Intelligent Buoy (GIB) can also be deployed for high accuracy if the work site is sufficiently close to the surface, although that is not always the case. In this paper, an LBL system is chosen to aid the a system composed by an IMU and AHRS.

An evidence of high accuracy and reliability with LBL systems is a recent patent [6], which describes a system that provides location information using multiple assemblies of IMUs paired with long baseline accelerometers and GNSS. In [8], a Bayesian near-real-time (NRT) state estimation approach with LBL transceivers is proposed for underwater inertial navigation. The solution combines filtering and smoothing for the nonlinear measurement model with asynchronous LBL measurements, conveying a real-time state estimate, suitable for planning and control purposes.

An LBL localization solution based on an extended Kalman filter and a real-time smoother is presented in [27], which was tested in a simulation environment and in field experiments with an underwater glider. A 3D compass conveys measurements of attitude and tilt angle of the vehicle, and there is a GPS unit to obtain a position fix when it surfaces. Globally exponentially stable position and linear velocity filters based on LBL have been presented in [2]. A bias added to the pseudo-ranges was also estimated, along with the inertial current velocity. However, the problem framework considers a Acoustic Doppler Current Profiler (ADCP), which measures the velocity of the vehicle relative to the fluid. Globally exponentially stable filters for the position, linear-velocity, and gravity acceleration on continuous time, with data from an IMU and AHRS in sensor-based LBL navigation have been presented in [4], where the range measurements are not corrupted by additive bias.

An acoustic navigation system relies on measuring distances based on the travel time of an acoustic signal. In one-way-travel-time mode, the travel time is computed as the difference between the time that the signal was emitted and the time that it was received. Therefore, there are measurement errors associated to the differences between the time in the emitter's and the receivers' clocks. Even if initially set to the same time, the rate that the clocks count time is different and will create, over time, a clock drift. Therefore, clock synchronization is important to accurately measure ranges, that is, to minimize the bias in the pseudo-ranges that results from the offset between the receiver's and emitters' clocks.

An application of asynchronous Kalman filtering to an underwater system consisting of an INS aided by a Doppler Velocity Log, an inclinometer, and a depth meter is presented in [22], where a field test was performed. Estimating variables of interest in a nonlinear system using an unscented Kalman filter is proposed in [17], where the authors mention its advantages in softening the dynamics of a single degree-of-freedom system.

Developments have been made towards implementing a node-based LBL system, called Dynamic Long Baseline (DLBL), where there is no distinction between receivers and emitters, as presented by the author in [11]. Such a configuration allows for all nodes in an underwater network to have localization capabilities.

Target localization using LBL positioning system was introduced in [31]. The authors propose an algorithm that initially calibrates the position of the beacon based on GPS measurements of a survey ship. The position calibration performs, although not ideally, clock synchronization. After having the calibrated positions, the target, with the same clock time as the survey ship, can estimate its position with the on-board navigation system. Field tests were performed, and the results of the LBL positioning system were compared against the position obtained with GPS.

Other underwater navigation systems besides acoustic have been recently studied, with the first example being sonar imaging localization, as seen in [13]. While localization using light-emitting diode (LED) has been

studied for scenarios on land, as seen in [32], and [14], LED underwater localization is a recent approach, as evidenced in [23], and will experience developments in the coming years. Simultaneous localization and mapping (SLAM), especially useful in AUV, consists of a machine mapping the environment and localizing itself in this environment, and has been an active topic of research. SLAM techniques, although out of scope of this paper, can also be envisioned. AUV navigation, localization, and challenges faced can be seen in [20], where camera-based localization is also discussed.

Efforts to synchronize the clocks of receivers and emitters have been performed, as seen in [1] for the LBL, and presented in [25], for a GPS-aided INS, where the clocks' offset was considered a state of interest, i.e., was estimated along with the position, velocity, and attitude of the vehicle.

The main objective of this paper is the development of a novel navigation system for LBL navigation aided by an IMU and an AHRS, that includes the estimation of a bias, considered to be constant, which accounts for the effect of the unknown offset between the clocks of the acoustic emitters and receivers. Therefore, the burden of initial clock synchronization is removed. The pseudo-ranges measured from the sensors consist of range measurements corrupted by an additive constant factor. These low-rate measurements allow to decrease the estimation error to values close to zero, using feedback, whereas the higher rate AHRS and IMU measurements drive the vehicle dynamics and are integrated in open-loop. A dynamic nonlinear model of the system, using pseudo-ranges, is derived and used in the observer design.

The estimation solution begins by performing system augmentation, considering the LBL configuration, allowing to design an augmented system that can be regarded as linear for observability analysis and observer design purposes. Observability analysis is then performed in order to design an observer that conveys globally exponentially stable error dynamics. Its performance is tested with Monte Carlo simulations. The main difference between the problem addressed in this paper and the one in [2] is that, in the former, a ADCP was considered, whereas in this paper an IMU is considered, thus increasing the order of the system dynamics and overall complexity.

The unknown offset between the clocks of the acoustic receivers and emitters is assumed constant, that is, the clocks of the beacons disposed in the LBL configuration are synchronized externally. To perform such a task, the beacons could be aided by a GPS receiver and distribute their measured fixed positions in the network, constantly updating their clocks such that they could be assumed as synchronized. A clock synchronization algorithm for *Ad Hoc* underwater acoustic systems that takes into account the limitations of using acoustic signals is proposed in [29]. Tools that measure the clock offset between underwater acoustic modems and allow for accurate clock synchronization are shown and expanded in [15]. A localization solution within a scenario in which the nodes are not time-synchronized and permanently moving, with the propagation speed of the acoustic signals unknown, is devised in [10].

Previous work by the authors can be found in the short conference paper [24], where the problem framework was first introduced and an estimation solution was briefly described. This paper presents the extensive derivation of the results and the proofs that had been omitted. Additionally, it also includes a thorough evaluation of the performance of the proposed solution, including Monte Carlo simulations and a comparison with the extended Kalman filter, the unscented Kalman filter, and the Bayesian Cramér-Rao bound.

2 Problem statement and notation

2.1 Notation

Throughout the paper, scalars, vectors and matrices are represented by a lowercase letter, a bold lowercase letter, and a bold uppercase letter, respectively. The symbol $\mathbf{0}_{n\times m}$ denotes a $n\times m$ matrix of zeros, $\mathbf{I}_n$ an identity matrix with dimension $n \times n$, and $\mathbf{diag}(\mathbf{A}_1, \ldots, \mathbf{A}_n)$ a block diagonal matrix. When the matrix dimensions are omitted, the matrices are assumed of appropriate dimensions. Given two vectors $\mathbf{x} \in \mathbb{R}^3$ and $\mathbf{y} \in \mathbb{R}^3$, $\mathbf{x} \times \mathbf{y}$ and $\mathbf{x} \cdot \mathbf{y}$ represent, respectively, the cross and inner products.

2.2 Problem statement

Consider an underwater vehicle moving in a scenario where a set of landmarks with fixed and known positions are laid out in a LBL configuration. Further suppose that the vehicle is equipped with an IMU, consisting of two triads of orthogonally mounted accelerometers and rate gyros and an AHRS. Fig. 1 depicts the aforementioned scenario.

2.2.1 System dynamics

Let {I} denote a local inertial reference frame, such as the North-East-Down (NED) frame, and {B} a body-fixed reference frame. The linear motion of the vehicle

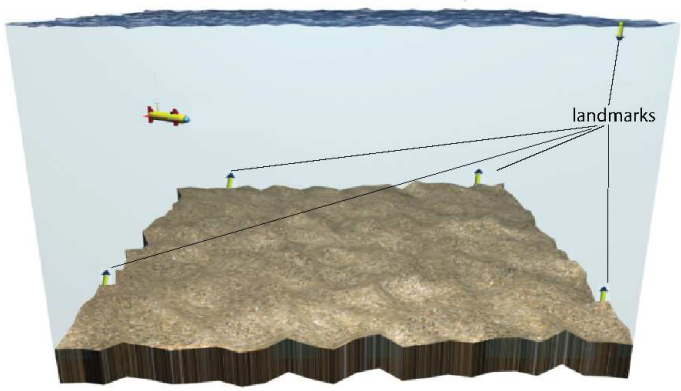

Fig. 1: Underwater LBL scenario

respects

$$\dot{\mathbf{p}}(t) = \mathbf{R}(t)\mathbf{v}(t), \tag{1}$$

where $\mathbf{p}(t) \in \mathbb{R}^3$ is the inertial position of the vehicle, $\mathbf{v}(t) \in \mathbb{R}^3$ is the velocity of the vehicle relative to the reference frame $\{\mathrm{I}\}$ expressed in the body-fixed reference frame $\{\mathrm{B}\}$, and $\mathbf{R}(t)$ is the rotation matrix from the reference frame $\{\mathrm{B}\}$ to $\{\mathrm{I}\}$, which satisfies $\dot{\mathbf{R}}(t) = \mathbf{R}(t)\mathbf{S}(\boldsymbol{\omega}(t))$, where $\boldsymbol{\omega}(t) \in \mathbb{R}^3$ is the angular velocity of the vehicle expressed in the reference frame $\{\mathrm{B}\}$ and $\mathbf{S}(\boldsymbol{\omega}(t))$ is the skew-symmetric matrix such that $\mathbf{S}(\boldsymbol{\omega}(t))\mathbf{x} = \boldsymbol{\omega} \times \mathbf{x}$. The rotation matrix $\mathbf{R}(t)$ and the angular velocity $\boldsymbol{\omega}(t)$ are provided by the AHRS. The IMU, which is assumed to be located at the center of mass of the vehicle, measures the linear acceleration $\mathbf{a}(t)$, given by

$$\mathbf{a}(t) = \dot{\mathbf{v}}(t) + \mathbf{S}(\boldsymbol{\omega}(t))\mathbf{v}(t) - \mathbf{g}(t), \tag{2}$$

where $\mathbf{g}(t) \in \mathbb{R}^3$ denotes the acceleration of gravity expressed in the reference frame $\{\mathrm{B}\}$. This term must be considered due to the inherent physics of non-ideal accelerometers, see [16] for further details. It would be possible to cancel out this term in (2), since the magnitude of $\mathbf{g}(t)$ is usually well-known. However, since even small errors on the rotation matrix $\mathbf{R}(t)$ would lead to large errors in the estimated acceleration, the acceleration of gravity $\mathbf{g}(t)$ is considered to be an unknown state, such as $\mathbf{p}(t)$ and $\mathbf{v}(t)$. The term $\mathbf{S}(\boldsymbol{\omega}(t))\mathbf{v}(t)$ represents the Coriolis acceleration. Finally, given the positions $\mathbf{s}_i \in \mathbb{R}^3, i = 1, \ldots, L$, of the landmarks, let $b_c(t)$ be the bias term that accounts for the effect of the unknown offset of the clocks between the emitters and receivers. The pseudo-range measurements are given by

$$r_i(k) = \|\mathbf{s}_i - \mathbf{p}(t_k)\| + b_c(t_k), \tag{3}$$

$i = 1, \ldots, L$, with $t_k := t_0 + kT, k \in \mathbb{N}$, where $T > 0$ is the sampling period and t_0 is the initial time. The following assumptions are considered.

Assumption 1 *The pseudo-range measurements are positive, i.e., $r_i(k) > 0, \forall k = 1, \ldots, L$.*

Assumption 2 *The offset of the clocks between the emitters and the receiver is constant, i.e., $\dot{b}_c(t) = 0$.*

Although drift is not considered in this paper, a possible drift on the clocks' offset can be accommodated by adjusting the parameters of the filters, as long as the drift is small. Alternatively, the system can also be augmented to accommodate for clock drift with a simple integrator.

The derivative of the acceleration of gravity is considered to be constant in inertial coordinates, which gives, in body-fixed coordinates,

$$\dot{\mathbf{g}}(t) = -\mathbf{S}(\boldsymbol{\omega}(t))\mathbf{g}(t). \tag{4}$$

Combining (1) and (3) to (4), as well as Assumption 2, yields the nonlinear system

$$\begin{cases} \dot{\mathbf{p}}(t) = \mathbf{R}(t)\mathbf{v}(t) \\ \dot{\mathbf{v}}(t) = \mathbf{a}(t) - \mathbf{S}(\boldsymbol{\omega}(t))\mathbf{v}(t) + \mathbf{g}(t) \\ \dot{\mathbf{g}}(t) = -\mathbf{S}(\boldsymbol{\omega}(t))\mathbf{g}(t) \\ \dot{b}_c(t) = 0 \\ r_1(k) = \|\mathbf{s}_1 - \mathbf{p}(t_k)\| + b_c(t_k) \\ \vdots \\ r_L(k) = \|\mathbf{s}_L - \mathbf{p}(t_k)\| + b_c(t_k) \end{cases} . \tag{5}$$

The problem addressed in this paper is the design of an estimation solution for (5).

2.2.2 Long baseline configuration

The LBL configuration has been widely used in the past in the design of navigation systems. In the remainder of the article, the following assumption is considered.

Assumption 3 *There exist at least 5 noncoplanar landmarks.*

In the case of at least four noncoplanar landmarks, it is possible to obtain the position of a vehicle from range measurements. Given that the measurements obtained from the sensors are corrupted with bias, which adds another variable to be estimated, an extra landmark is considered in order to guarantee estimation.

3 Filter design

3.1 State transformation and discretization

Let $\mathbf{T}(t) := \mathbf{diag}(\mathbf{I}, \mathbf{R}(t), \mathbf{R}(t), 1) \in \mathbb{R}^{10\times 10}$ be a Lyapunov state transformation, previously used in [3], and consider the state transformation

$$\begin{bmatrix}\mathbf{z}_1(t)\\ \mathbf{z}_2(t)\\ \mathbf{z}_3(t)\\ z_4(t)\end{bmatrix} := \mathbf{T}(t)\begin{bmatrix}\mathbf{p}(t)\\ \mathbf{v}(t)\\ \mathbf{g}(t)\\ b_c(t)\end{bmatrix}. \tag{6}$$

Then, the new system dynamics can be written as

$$\begin{cases}\dot{\mathbf{z}}_1(t) = \mathbf{z}_2(t)\\ \dot{\mathbf{z}}_2(t) = \mathbf{z}_3(t) + \mathbf{R}(t)\mathbf{a}(t)\\ \dot{\mathbf{z}}_3(t) = \mathbf{0}\\ \dot{z}_4(t) = 0\\ r_1(k) = \|\mathbf{s}_1 - \mathbf{z}_1(t_k)\| + z_4(t_k)\\ \vdots\\ r_L(k) = \|\mathbf{s}_L - \mathbf{z}_1(t_k)\| + z_4(t_k)\end{cases}. \tag{7}$$

Since (6) is a Lyapunov transformation, all observability properties are preserved (see [7]). Implementing the state transformation (6) is advantageous as the new system (7), albeit still nonlinear, is now time invariant, considering $\mathbf{R}(t)\mathbf{a}(t)$ as an input. Considering only the first four states, exact discretization is performed, which yields

$$\begin{cases}\mathbf{z}_1(t_{k+1}) = \mathbf{z}_1(t_k) + T\mathbf{z}_2(t_k) + \frac{T^2}{2}\mathbf{z}_3(t_k) + \\ \qquad + \int_{t_k}^{t_{k+1}} (t_{k+1}-\tau)\mathbf{R}(\tau)\mathbf{a}(\tau)d\tau\\ \mathbf{z}_2(t_{k+1}) = \mathbf{z}_2(t_k) + T\mathbf{z}_3(t_k) + \int_{t_k}^{t_{k+1}} \mathbf{R}(\tau)\mathbf{a}(\tau)d\tau\\ \mathbf{z}_3(t_{k+1}) = \mathbf{z}_3(t_k)\\ z_4(t_{k+1}) = z_4(t_k)\end{cases}. \tag{8}$$

Inverting the Lyapunov transformation, in discrete-time, gives $\mathbf{T}^{-1}(t_k) = \mathbf{diag}(\mathbf{I}, \mathbf{R}^T(t_k), \mathbf{R}^T(t_k), 1)$, since the rotation matrix is orthonormal, i.e. $\mathbf{R}^{-1}(t) = \mathbf{R}^T(t)$. This transformation can then be applied to (8) and discrete-time states can be defined, that is,

$$\begin{bmatrix}\mathbf{x}_1(k)\\ \mathbf{x}_2(k)\\ \mathbf{x}_3(k)\\ x_4(k)\end{bmatrix} := \begin{bmatrix}\mathbf{p}(t_k)\\ \mathbf{v}(t_k)\\ \mathbf{g}(t_k)\\ b_c(t_k)\end{bmatrix} = \mathbf{T}^{-1}(t_k)\begin{bmatrix}\mathbf{z}_1(t_k)\\ \mathbf{z}_2(t_k)\\ \mathbf{z}_3(t_k)\\ z_4(t_k)\end{bmatrix}.$$

After re-introducing the pseudo-range measurements, the discrete-time system dynamics can be written as

$$\begin{cases}\mathbf{x}_1(k+1) = \mathbf{x}_1(k) + T\mathbf{R}(t_k)\mathbf{x}_2(k) + \frac{T^2}{2}\mathbf{R}(t_k)\mathbf{x}_3(k)\\ \qquad + \mathbf{u}_1(k)\\ \mathbf{x}_2(k+1) = \mathbf{R}^T(t_{k+1})\mathbf{R}(t_k)\mathbf{x}_2(k)\\ \qquad + T\mathbf{R}^T(t_{k+1})\mathbf{R}(t_k)\mathbf{x}_3(k) + \mathbf{u}_2(k)\\ \mathbf{x}_3(k+1) = \mathbf{R}^T(t_{k+1})\mathbf{R}(t_k)\mathbf{x}_3(k)\\ x_4(k+1) = x_4(k)\\ r_1(k) = \|\mathbf{s}_1 - \mathbf{x}_1(k)\| + x_4(k)\\ \vdots\\ r_L(k) = \|\mathbf{s}_L - \mathbf{x}_1(k)\| + x_4(k)\end{cases}, \tag{9}$$

where $\mathbf{u}_1(k) = \int_{t_k}^{t_{k+1}} (t_{k+1}-\tau)\mathbf{R}(\tau)\mathbf{a}(\tau)d\tau$ and $\mathbf{u}_2(k) = \mathbf{R}^T(t_{k+1})\int_{t_k}^{t_{k+1}} \mathbf{R}(\tau)\mathbf{a}(\tau)d\tau$.

3.2 State augmentation

As a function of the system states in (9), the pseudo-ranges are given by $r_i(k) = \|\mathbf{s}_i - \mathbf{x}_1(k)\| + x_4(k), \quad i = 1, \ldots, L$. To encode the LBL structure, the difference of pseudo-ranges measured to two different beacons is computed [2], which gives

$$\begin{aligned} r_i(k) - r_j(k) = &-2\frac{\mathbf{s}_i - \mathbf{s}_j}{r_i(k) + r_j(k)} \cdot \mathbf{x}_1(k) + \\ &+ 2\frac{r_i(k) - r_j(k)}{r_i(k) + r_j(k)}x_4(k) + \frac{\|\mathbf{s}_i\|^2 - \|\mathbf{s}_j\|^2}{r_i(k) + r_j(k)}, \end{aligned} \tag{10}$$

for $i, j \in \{1, \ldots, L\}, i \neq j$. This approach is the same as the one presented in [2], albeit with different state transition equations. These differences are defined as new states,

$$\begin{bmatrix}x_5(k)\\ x_6(k)\\ \vdots\\ x_{3+C_2^L}(k)\\ x_{4+C_2^L}(k)\end{bmatrix} := \begin{bmatrix}r_1(k) - r_2(k)\\ r_1(k) - r_3(k)\\ \vdots\\ r_{L-2}(k) - r_L(k)\\ r_{L-1}(k) - r_L(k)\end{bmatrix},$$

where C_2^L is the number of 2-combinations for a set of L elements, i.e., $C_2^L = \frac{L(L-1)}{2}$. To obtain the state transition equation for the pseudo-range differences, (10) is re-written for $k = k+1$, and (9) is used to expand it,

which gives

$$
\begin{aligned}
r_i(k+1) - r_j(k+1) &= \frac{-2(\mathbf{s}_i - \mathbf{s}_j)^T}{r_i(k+1)+r_j(k+1)}\mathbf{x}_1(k+1) \\
&+ 2\frac{r_i(k+1)-r_j(k+1)}{r_i(k+1)+r_j(k+1)}x_4(k+1) + \frac{\|\mathbf{s}_i\|^2 - \|\mathbf{s}_j\|^2}{r_i(k+1)+r_j(k+1)} \\
&= \frac{-2(\mathbf{s}_i - \mathbf{s}_j)^T}{r_i(k+1)+r_j(k+1)}\left[\mathbf{x}_1(k) + T\mathbf{R}(t_k)\mathbf{x}_2(k)\right] \\
&+ \frac{-2(\mathbf{s}_i - \mathbf{s}_j)^T}{r_i(k+1)+r_j(k+1)}\left[\frac{T^2}{2}\mathbf{R}(t_k)\mathbf{x}_3(k) + \mathbf{u}_1(k)\right] \\
&+ 2\frac{r_i(k+1)-r_j(k+1)}{r_i(k+1)+r_j(k+1)}x_4(k) + \frac{\|\mathbf{s}_i\|^2 - \|\mathbf{s}_j\|^2}{r_i(k+1)+r_j(k+1)}.
\end{aligned} \tag{11}
$$

To remove the independent term, using (10) and Assumption 1 gives

$$
\begin{aligned}
&\frac{r_i(k)+r_j(k)}{r_i(k+1)+r_j(k+1)}[r_i(k)-r_j(k)] = \\
&\frac{-2(\mathbf{s}_i - \mathbf{s}_j)^T}{r_i(k+1)+r_j(k+1)}\mathbf{x}_1(k) + 2\frac{r_i(k)-r_j(k)}{r_i(k+1)+r_j(k+1)}x_4(k) \\
&+ \frac{\|\mathbf{s}_i\|^2 - \|\mathbf{s}_j\|^2}{r_i(k+1)+r_j(k+1)}.
\end{aligned}
$$

Substituting this in (11) gives

$$
\begin{aligned}
&r_i(k+1) - r_j(k+1) = \\
&\frac{r_i(k)+r_j(k)}{r_i(k+1)+r_j(k+1)}[r_i(k)-r_j(k)] + \\
&2\frac{r_i(k+1)-r_j(k+1)}{r_i(k+1)+r_j(k+1)}x_4(k) - \\
&2\frac{r_i(k)-r_j(k)}{r_i(k+1)+r_j(k+1)}x_4(k) \\
&+ \frac{-2(\mathbf{s}_i - \mathbf{s}_j)^T}{r_i(k+1)+r_j(k+1)}\Bigg[T\mathbf{R}(t_k)\mathbf{x}_2(k) + \\
&\frac{T^2}{2}\mathbf{R}(t_k)\mathbf{x}_3(k) + \mathbf{u}_1(k)\Bigg].
\end{aligned}
$$

The pseudo-range state transition equation can then be re-written as

$$
\begin{aligned}
r_i(k+1) - r_j(k+1) &= \frac{-2(\mathbf{s}_i - \mathbf{s}_j)^T T\mathbf{R}(t_k)}{r_i(k+1)+r_j(k+1)}\mathbf{x}_2(k) \\
&+ \frac{-(\mathbf{s}_i - \mathbf{s}_j)^T T^2\mathbf{R}(t_k)}{r_i(k+1)+r_j(k+1)}\mathbf{x}_3(k) \\
&+ \frac{2\left[(r_i(k+1)-r_i(k)) - (r_j(k+1)-r_j(k))\right]}{r_i(k+1)+r_j(k+1)}x_4(k) \\
&+ \frac{r_i(k)+r_j(k)}{r_i(k+1)+r_j(k+1)}\left[r_i(k)-r_j(k)\right] \\
&+ \frac{-2(\mathbf{s}_i - \mathbf{s}_j)^T}{r_i(k+1)+r_j(k+1)}\mathbf{u}_1(k).
\end{aligned}
$$

The augmented state vector is then defined as

$$
\mathbf{x}(k) := \begin{bmatrix} \mathbf{x}_1(k) \\ \mathbf{x}_2(k) \\ \mathbf{x}_3(k) \\ x_4(k) \\ x_5(k) \\ \vdots \\ x_{4+C_2^L}(k) \end{bmatrix} \in \mathbb{R}^{10+C_2^L}. \tag{13}
$$

The state dynamic equation for the augmented state vector can then be written, in compact form, as

$$
\mathbf{x}(k+1) = \mathbf{A}(k)\mathbf{x}(k) + \mathbf{B}\mathbf{u}_a(k),
$$

where $\mathbf{A}(k) \in \mathbb{R}^{(10+C_2^L)\times(10+C_2^L)}$ is defined as

$$
\mathbf{A}(k) = \begin{bmatrix} \mathbf{A}_{11}(k) & \mathbf{0}_{10\times C_2^L} \\ \mathbf{A}_{21}(k) & \mathbf{A}_{22}(k) \end{bmatrix},
$$

with $\mathbf{A}_{11}(k) \in \mathbb{R}^{10\times 10}$, $\mathbf{A}_{21}(k) \in \mathbb{R}^{C_2^L\times 10}$ and $\mathbf{A}_{22}(k) \in \mathbb{R}^{C_2^L\times C_2^L}$, $\mathbf{B} \in \mathbb{R}^{(10+C_2^L)\times(6+C_2^L)}$ given by

$$
\mathbf{A}_{11}(k) = \begin{bmatrix} \mathbf{I} & T\mathbf{R}(t_k) & \frac{T^2}{2}\mathbf{R}(t_k) & \mathbf{0}_{3\times 1} \\ \mathbf{0}_3 & \mathbf{R}^T(t_{k+1})\mathbf{R}(t_k) & T\mathbf{R}^T(t_{k+1})\mathbf{R}(t_k) & \mathbf{0}_{3\times 1} \\ \mathbf{0}_3 & \mathbf{0}_3 & \mathbf{R}^T(t_{k+1})\mathbf{R}(t_k) & \mathbf{0}_{3\times 1} \\ \mathbf{0}_{1\times 3} & \mathbf{0}_{1\times 3} & \mathbf{0}_{1\times 3} & 1 \end{bmatrix},
$$

$$
\mathbf{A}_{21}(k) = \begin{bmatrix} \mathbf{0}_{1\times 3} & \frac{-2(\mathbf{s}_1-\mathbf{s}_2)^T T\mathbf{R}(t_k)}{r_1(k+1)+r_2(k+1)} & \frac{-(\mathbf{s}_1-\mathbf{s}_2)^T T^2\mathbf{R}(t_k)}{r_1(k+1)+r_2(k+1)} \\ \mathbf{0}_{1\times 3} & \frac{-2(\mathbf{s}_1-\mathbf{s}_3)^T T\mathbf{R}(t_k)}{r_1(k+1)+r_3(k+1)} & \frac{-(\mathbf{s}_1-\mathbf{s}_3)^T T^2\mathbf{R}(t_k)}{r_1(k+1)+r_3(k+1)} \\ \vdots & \vdots & \vdots \\ \mathbf{0}_{1\times 3} & \frac{-2(\mathbf{s}_{L-2}-\mathbf{s}_L)^T T\mathbf{R}(t_k)}{r_{L-2}(k+1)+r_L(k+1)} & \frac{-(\mathbf{s}_{L-2}-\mathbf{s}_L)^T T^2\mathbf{R}(t_k)}{r_{L-2}(k+1)+r_L(k+1)} \\ \mathbf{0}_{1\times 3} & \frac{-2(\mathbf{s}_{L-1}-\mathbf{s}_L)^T T\mathbf{R}(t_k)}{r_{L-1}(k+1)+r_L(k+1)} & \frac{-(\mathbf{s}_{L-1}-\mathbf{s}_L)^T T^2\mathbf{R}(t_k)}{r_{L-1}(k+1)+r_L(k+1)} \end{bmatrix},
$$

$$
\begin{bmatrix} \frac{2[(r_1(k+1)-r_1(k))-(r_2(k+1)-r_2(k))]}{r_1(k+1)+r_2(k+1)} \\ \frac{2[(r_1(k+1)-r_1(k))-(r_3(k+1)-r_3(k))]}{r_1(k+1)+r_3(k+1)} \\ \vdots \\ \frac{2[(r_{L-2}(k+1)-r_{L-2}(k))-(r_L(k+1)-r_L(k))]}{r_{L-2}(k+1)+r_L(k+1)} \\ \frac{2[(r_{L-1}(k+1)-r_{L-1}(k))-(r_L(k+1)-r_L(k))]}{r_{L-1}(k+1)+r_L(k+1)} \end{bmatrix}
$$

$$
\begin{aligned}
\mathbf{A}_{22}(k) = \mathbf{diag}\Bigg(&\frac{r_1(k)+r_2(k)}{r_1(k+1)+r_2(k+1)}, \\
&\frac{r_1(k)+r_3(k)}{r_1(k+1)+r_3(k+1)}, \ldots, \\
&\frac{r_{L-2}(k)+r_L(k)}{r_{L-2}(k+1)+r_L(k+1)}, \\
&\frac{r_{L-1}(k)+r_L(k)}{r_{L-1}(k+1)+r_L(k+1)}\Bigg)
\end{aligned},
$$

$$\mathbf{B} = \begin{bmatrix} \mathbf{I}_3 & \mathbf{0}_3 & \mathbf{0}_{3\times C_2^L} \\ \mathbf{0}_3 & \mathbf{I}_3 & \mathbf{0}_{3\times C_2^L} \\ \mathbf{0}_3 & \mathbf{0}_3 & \mathbf{0}_{3\times C_2^L} \\ \mathbf{0}_{1\times 3} & \mathbf{0}_{1\times 3} & \mathbf{0}_{1\times C_2^L} \\ \mathbf{0}_{C_2^L\times 3} & \mathbf{0}_{C_2^L\times 3} & \mathbf{I}_{C_2^L} \end{bmatrix},$$

and

$$\mathbf{u}_a(k) = \begin{bmatrix} \mathbf{u}_1(k) \\ \mathbf{u}_2(k) \\ \frac{-2(\mathbf{s}_1-\mathbf{s}_2)^T}{r_1(k+1)+r_2(k+1)}\mathbf{u}_1(k) \\ \frac{-2(\mathbf{s}_1-\mathbf{s}_3)^T}{r_1(k+1)+r_3(k+1)}\mathbf{u}_1(k) \\ \vdots \\ \frac{-2(\mathbf{s}_{L-2}-\mathbf{s}_L)^T}{r_{L-2}(k+1)+r_L(k+1)}\mathbf{u}_1(k) \\ \frac{-2(\mathbf{s}_{L-1}-\mathbf{s}_L)^T}{r_{L-1}(k+1)+r_L(k+1)}\mathbf{u}_1(k) \end{bmatrix} \in \mathbb{R}^{6+C_2^L}.$$

Discarding the original nonlinear output, noticing that the states $x_5(k), \dots x_{4+C_2^L}(k)$ are available, and using (10), define the augmented discrete-time system, in compact form,

$$\begin{cases} \mathbf{x}(k+1) = \mathbf{A}(k)\mathbf{x}(k) + \mathbf{B}\mathbf{u}_a(k) \\ \mathbf{y}(k+1) = \mathbf{C}(k+1)\mathbf{x}(k+1) \end{cases}, \tag{14}$$

where $\mathbf{C}(k) \in \mathbb{R}^{2C_2^L\times(10+C_2^L)}$ is defined as

$$\mathbf{C}(k) = \begin{bmatrix} \mathbf{0} & \mathbf{0}\,\mathbf{0} & 0 & \mathbf{I} \\ \mathbf{C}_{21}(k) & \mathbf{0}\,\mathbf{0} & \mathbf{C}_{24}(k) & \mathbf{I} \end{bmatrix},$$

with $\mathbf{C}_{21}(k) \in \mathbb{R}^{C_2^L\times 3}$ and $\mathbf{C}_{24}(k) \in \mathbb{R}^{C_2^L}$ given by

$$\mathbf{C}_{21}(k) = \begin{bmatrix} 2\frac{(\mathbf{s}_1-\mathbf{s}_2)^T}{r_1(k)+r_2(k)} \\ 2\frac{(\mathbf{s}_1-\mathbf{s}_3)^T}{r_1(k)+r_3(k)} \\ \vdots \\ 2\frac{(\mathbf{s}_{L-2}-\mathbf{s}_L)^T}{r_{L-2}(k)+r_L(k)} \\ 2\frac{(\mathbf{s}_{L-1}-\mathbf{s}_L)^T}{r_{L-1}(k)+r_L(k)} \end{bmatrix},$$

and

$$\mathbf{C}_{24}(k) = \begin{bmatrix} -2\frac{r_1(k)-r_2(k)}{r_1(k)+r_2(k)} \\ -2\frac{r_1(k)-r_3(k)}{r_1(k)+r_3(k)} \\ \vdots \\ -2\frac{r_{L-2}(k)-r_L(k)}{r_{L-2}(k)+r_L(k)} \\ -2\frac{r_{L-1}(k)-r_L(k)}{r_{L-1}(k)+r_L(k)} \end{bmatrix}.$$

Notice that $\mathbf{C}_{21}(k)$ and $\mathbf{C}_{24}(k)$ were defined to encode (10).

3.3 Observability analysis

The discrete time-varying system (14) can still be considered linear in the state for observer design purposes, even though the system matrices $\mathbf{A}(k)$ and $\mathbf{C}(k)$ depend on the pseudo-range measurements. This is possible because the pseudo-range measurements are assumed to be available, and therefore are considered as functions of time for observer (or filter) design purposes.

Theorem 1 and Theorem 2 address, respectively, the observability of the discrete-time system (14) and the observability of the nonlinear system (9).

Theorem 1 *Suppose that the LBL acoustic configuration is such that, for some $k_i \geq k_0$, under Assumption 3, the matrix*

$$\mathbf{L}(k_i) = \begin{bmatrix} (\mathbf{s}_1-\mathbf{s}_2)^T & -[r_1(k_i)-r_2(k_i)] \\ (\mathbf{s}_1-\mathbf{s}_3)^T & -[r_1(k_i)-r_3(k_i)] \\ \vdots & \vdots \\ (\mathbf{s}_{L-2}-\mathbf{s}_L)^T & -[r_{L-2}(k_i)-r_L(k_i)] \\ (\mathbf{s}_{L-1}-\mathbf{s}_L)^T & -[r_{L-1}(k_i)-r_L(k_i)] \end{bmatrix}$$

is full rank, i.e.,

$$rank(\mathbf{L}(k_i)) = 4. \tag{15}$$

Then, the discrete-time system is observable on the interval $[k_i, k_i+3]$, in the sense that the initial state $\mathbf{x}(k_i)$ is uniquely determined by the input $\{\mathbf{u}(k) : k = k_i, k_i+1, k_i+2\}$ and the output $\{\mathbf{y}(k) : k = k_i, k_i+1, k_i+2\}$.

Proof The proof reduces to demonstrating that the observability matrix $\mathcal{O}(k_i, k_i+3)$ associated with the pair $(\mathbf{A}(k), \mathbf{C}(k))$ on $[k_i, k_i+3], k_i \geq k_0$ has rank equal to the number of states of the system. This can be done by showing that the contradiction is impossible. Fix $k_i \geq k_0$ and suppose that the rank of $\mathcal{O}(k_i, k_i+3)$ is less than the number of states of the system while assuming that (15) holds. Then, there exists a unit vector $\mathbf{d} = [\mathbf{d}_1^T \mathbf{d}_2^T \mathbf{d}_3^T d_4 \mathbf{d}_5^T]^T \in \mathbb{R}^{10+C_2^L}$, with $\mathbf{d}_1 \in \mathbb{R}^3$, $\mathbf{d}_2 \in \mathbb{R}^3$, $\mathbf{d}_3 \in \mathbb{R}^3$, $d_4 \in \mathbb{R}$, and $\mathbf{d}_5 \in \mathbb{R}^{C_2^L}$, such that $\mathcal{O}(k_i, k_i+3)\mathbf{d} = \mathbf{0}$, or, equivalently,

$$\begin{cases} \mathbf{C}(k_i)\mathbf{d} = \mathbf{0} \\ \mathbf{C}(k_i+1)\mathbf{A}(k_i)\mathbf{d} = \mathbf{0} \\ \mathbf{C}(k_i+2)\mathbf{A}(k_i+1)\mathbf{A}(k_i)\mathbf{d} = \mathbf{0} \end{cases}. \tag{16}$$

From the first equation of (16) and attending to the structure of $\mathbf{C}(k)$, one concludes that $\mathbf{d}_5 = \mathbf{0}$. Substi-

tuting that in the first equation of (16) results in

$$\begin{cases} \frac{2(\mathbf{s}_1-\mathbf{s}_2)^T\mathbf{d}_1-[r_1(k_i)-r_2(k_i)]d_4}{r_1(k_i)+r_2(k_i)}=0 \\ \frac{2(\mathbf{s}_1-\mathbf{s}_3)^T\mathbf{d}_1-[r_1(k_i)-r_3(k_i)]d_4}{r_1(k_i)+r_3(k_i)}=0 \\ \vdots \\ \frac{2(\mathbf{s}_{L-2}-\mathbf{s}_L)^T\mathbf{d}_1-[r_{L-2}(k_i)-r_L(k_i)]d_4}{r_{L-2}(k_i)+r_L(k_i)}=0 \\ \frac{2(\mathbf{s}_{L-1}-\mathbf{s}_L)^T\mathbf{d}_1-[r_{L-1}(k_i)-r_L(k_i)]d_4}{r_{L-1}(k_i)+r_L(k_i)}=0 \end{cases}. \tag{17}$$

Then, if (15) holds, the only solution of (17) is $\mathbf{d}_1=\mathbf{0}$ and $d_4=0$. Using $\mathbf{d}_5=\mathbf{0}$ as well, and substituting in the second equation of (16) gives

$$\begin{cases} \frac{-(\mathbf{s}_1-\mathbf{s}_2)^T T\mathbf{R}(t_{k_i})}{r_1(k_i+1)+r_2(k_i+1)}(2\mathbf{d}_2+T\mathbf{d}_3)=0 \\ \frac{-(\mathbf{s}_1-\mathbf{s}_3)^T T\mathbf{R}(t_{k_i})}{r_1(k_i+1)+r_3(k_i+1)}(2\mathbf{d}_2+T\mathbf{d}_3)=0 \\ \vdots \\ \frac{-(\mathbf{s}_{L-2}-\mathbf{s}_L)^T T\mathbf{R}(t_{k_i})}{r_{L-2}(k_i+1)+r_L(k_i+1)}(2\mathbf{d}_2+T\mathbf{d}_3)=0 \\ \frac{-(\mathbf{s}_{L-1}-\mathbf{s}_L)^T T\mathbf{R}(t_{k_i})}{r_{L-1}(k_i+1)+r_L(k_i+1)}(2\mathbf{d}_2+T\mathbf{d}_3)=0 \end{cases}. \tag{18}$$

Now, the third equation of (16) is used, which gives, considering also $\mathbf{d}_1=\mathbf{0}$, $d_4=0$, and $\mathbf{d}_5=\mathbf{0}$,

$$\begin{cases} \frac{-(\mathbf{s}_1-\mathbf{s}_2)^T T\mathbf{R}(t_{k_i})}{r_1(k_i+2)+r_2(k_i+2)}(2\mathbf{d}_2+2T\mathbf{d}_3)=0 \\ \frac{-(\mathbf{s}_1-\mathbf{s}_3)^T T\mathbf{R}(t_{k_i})}{r_1(k_i+2)+r_3(k_i+2)}(2\mathbf{d}_2+2T\mathbf{d}_3)=0 \\ \vdots \\ \frac{-(\mathbf{s}_{L-2}-\mathbf{s}_L)^T T\mathbf{R}(t_{k_i})}{r_{L-2}(k_i+2)+r_L(k_i+2)}(2\mathbf{d}_2+2T\mathbf{d}_3)=0 \\ \frac{-(\mathbf{s}_{L-1}-\mathbf{s}_L)^T T\mathbf{R}(t_{k_i})}{r_{L-1}(k_i+2)+r_L(k_i+2)}(2\mathbf{d}_2+2T\mathbf{d}_3)=0 \end{cases}. \tag{19}$$

Comparing (18) and (19) and noticing that the vectors $[2 \quad T]$ and $[2 \quad 2T]$ are linearly independent for $T\neq 0$, the only solution is $\mathbf{d}_2=\mathbf{0}$ and $\mathbf{d}_3=\mathbf{0}$. But this contradicts the initial hypothesis of the existence of a vector $\mathbf{d}\neq\mathbf{0}$ such that (16) holds. Therefore, the observability matrix must have rank equal to the number of states of the system, hence concluding the proof. □

Finally, it is important to note that when defining the system (14), the original nonlinear outputs $r_i(k)=\|\mathbf{s}_i-\mathbf{x}_1(k+1)\|+x_3(k), i=1,\ldots,L$, were discarded. Furthermore, there is nothing in (14) imposing the nonlinear constraints on the augmented states relating them with the original system states. Therefore, care must be taken when extrapolating observability conclusions of (14) to (9). Theorem 2 addresses this issue, providing the means for the design of a state observer or filter for (9).

Theorem 2 *Suppose that* (15) *holds for some* $k_i\geq k_0$. *Then:*

1. *the nonlinear system* (9) *is observable on the interval* $[k_i, k_i+3]$, *in the sense that the initial state* $x(k_i)$ *is uniquely determined by the input* $\{\mathbf{u}(k): k=k_i, k_i+1, k_i+2\}$ *and the output* $\{\mathbf{y}(k): k=k_i, k_i+1, k_i+2\}$.
2. *the initial condition of the augmented system* (14) *matches that of the nonlinear system* (9) *on the interval* $[k_i, k_i+3]$, *i.e.,*

$$\begin{cases} \mathbf{x}_1(k_i)=\mathbf{p}(t_{k_i}) \\ \mathbf{x}_2(k_i)=\mathbf{v}(t_{k_i}) \\ \mathbf{x}_3(k_i)=\mathbf{g}(t_{k_i}) \\ x_4(k_i)=b_c(t_{k_i}) \\ x_5(k_i)=\|\mathbf{s}_1-\mathbf{p}(t_{k_i})\|-\|\mathbf{s}_2-\mathbf{p}(t_{k_i})\| \\ x_6(k_i)=\|\mathbf{s}_1-\mathbf{p}(t_{k_i})\|-\|\mathbf{s}_3-\mathbf{p}(t_{k_i})\| \\ \vdots \\ x_{3+C_2^L}(k_i)=\|\mathbf{s}_{L-2}-\mathbf{p}(t_{k_i})\|-\|\mathbf{s}_L-\mathbf{p}(t_{k_i})\| \\ x_{4+C_2^L}(k_i)=\|\mathbf{s}_{L-1}-\mathbf{p}(t_{k_i})\|-\|\mathbf{s}_L-\mathbf{p}(t_{k_i})\| \end{cases}.$$

Proof Let

$$\mathbf{x}(k_i):=\begin{bmatrix} \mathbf{x}_1(k_i) \\ \mathbf{x}_2(k_i) \\ \mathbf{x}_3(k_i) \\ x_4(k_i) \\ x_5(k_i) \\ \vdots \\ x_{3+C_2^L}(k_i) \\ x_{4+C_2^L}(k_i) \end{bmatrix}\in\mathbb{R}^{3+3+3+1+C_2^L}$$

be the initial condition of the augmented system (14) and let $\mathbf{p}(t_{k_i})$, $\mathbf{v}(t_{k_i})$, $\mathbf{g}(t_{k_i})$ and $b_c(t_{k_i})$ be the initial condition of the initial system (9). From the first C_2^L outputs of the augmented system,

$$\begin{cases} x_5(k_i)=r_1(k_i)-r_2(k_i) \\ x_6(k_i)=r_1(k_i)-r_3(k_i) \\ \vdots \\ x_{3+C_2^L}(k_i)=r_{L-2}(k_i)-r_L(k_i) \\ x_{4+C_2^L}(k_i)=r_{L-1}(k_i)-r_L(k_i) \end{cases}. \tag{20}$$

The outputs from (20) are equivalent to

$$\begin{cases} x_5(k_i)=\|\mathbf{s}_1-\mathbf{p}(t_{k_i})\|-\|\mathbf{s}_2-\mathbf{p}(t_{k_i})\| \\ x_6(k_i)=\|\mathbf{s}_1-\mathbf{p}(t_{k_i})\|-\|\mathbf{s}_3-\mathbf{p}(t_{k_i})\| \\ \vdots \\ x_{3+C_2^L}(k_i)=\|\mathbf{s}_{L-2}-\mathbf{p}(t_{k_i})\|-\|\mathbf{s}_L-\mathbf{p}(t_{k_i})\| \\ x_{4+C_2^L}(k_i)=\|\mathbf{s}_{L-1}-\mathbf{p}(t_{k_i})\|-\|\mathbf{s}_L-\mathbf{p}(t_{k_i})\| \end{cases}.$$

Considering the differences in pseudo-range measurements of the nonlinear system (9) for $k = k_i$ as a function of the initial state gives

$$\begin{aligned} r_l(k_i) - r_m(k_i) &= -2\frac{\mathbf{s}_l - \mathbf{s}_m}{r_l(k_i) + r_m(k_i)} \cdot \mathbf{p}(t_{k_i}) \\ &+ 2\frac{r_l(k_i) - r_m(k_i)}{r_l(k_i) + r_m(k_i)} b_c(t_{k_i}) + \frac{\|\mathbf{s}_l\|^2 - \|\mathbf{s}_m\|^2}{r_l(k_i) + r_m(k_i)} \end{aligned}, \tag{21}$$

for all $l, m \in \{1, \ldots, L\}, l \neq m$. Evaluating the outputs of the augmented system (9) $\mathbf{y}_{C_2^L+1}(k)$ to $\mathbf{y}_{2C_2^L}(k)$ for $k = k_i$ as a function of the state $\mathbf{x}(k_i)$ and considering (20), gives

$$\begin{aligned} r_l(k_i) - r_m(k_i) &= -2\frac{\mathbf{s}_l - \mathbf{s}_m}{r_l(k_i) + r_m(k_i)} \cdot \mathbf{x}_1(t_{k_i}) \\ &+ 2\frac{r_l(k_i) - r_m(k_i)}{r_l(k_i) + r_m(k_i)} x_4(t_{k_i}) + \frac{\|\mathbf{s}_l\|^2 - \|\mathbf{s}_m\|^2}{r_l(k_i) + r_m(k_i)} \end{aligned}, \tag{22}$$

for all $l, m \in \{1, \ldots, L\}, l \neq m$. Comparing (21) and (22) allows to conclude, under the hypothesis of the theorem, that

$$\begin{cases} \mathbf{x}_1(k_i) = \mathbf{p}(t_{k_i}) \\ x_4(k_i) = b_c(t_{k_i}) \end{cases}. \tag{23}$$

It is possible to write the differences of pseudo-ranges for $k_i = k_i + 1$ as a function of the initial state of the nonlinear system (9), as given by

$$\begin{aligned} r_l(k_i+1) - r_m(k_i+1) &= \frac{\|\mathbf{s}_l\|^2 - \|\mathbf{s}_m\|^2}{r_l(k_i+1) + r_m(k_i+1)} \\ &- \frac{2(\mathbf{s}_l - \mathbf{s}_m)^T}{r_l(k_i+1) + r_m(k_i+1)} \left[\mathbf{p}(t_{k_i}) + T\mathbf{R}(t_{k_i})\mathbf{v}(t_{k_i})\right. \\ &\left. + \frac{T^2}{2}\mathbf{R}(t_{k_i})\mathbf{g}(t_{k_i}) + \mathbf{u}_1(k_i)\right] \\ &+ 2\frac{r_l(k_i+1) - r_m(k_i+1)}{r_l(k_i+1) + r_m(k_i+1)} b_c(t_{k_i}) \end{aligned}, \tag{24}$$

for all $l, m \in \{1, \ldots, L\}, l \neq m$. From the first L outputs of (14), for $k = k_i + 1$, and using (20), (22), and (23), it is possible to write, after some computations,

$$\begin{aligned} r_l(k_i+1) - r_m(k_i+1) &= \frac{\|\mathbf{s}_l\|^2 - \|\mathbf{s}_m\|^2}{r_l(k_i+1) + r_m(k_i+1)} \\ &- \frac{2(\mathbf{s}_l - \mathbf{s}_m)^T}{r_l(k_i+1) + r_m(k_i+1)} \left[\mathbf{p}(t_{k_i}) + T\mathbf{R}(t_{k_i})\mathbf{x}_2(t_{k_i})\right. \\ &\left. + \frac{T^2}{2}\mathbf{R}(t_{k_i})\mathbf{x}_3(t_{k_i}) + \mathbf{u}_1(k_i)\right] \\ &+ 2\frac{r_l(k_i+1) - r_m(k_i+1)}{r_l(k_i+1) + r_m(k_i+1)} b_c(t_{k_i}) \end{aligned} \tag{25}$$

for all $l, m \in \{1, \ldots, L\}, l \neq m$. Since comparing (25) and (24) does not allow for a conclusion, the differences of pseudo-ranges for $k_i = k_i + 2$ as a function of the initial state of the system (8) are computed, as given by

$$\begin{aligned} r_l(k_i+2) - r_m(k_i+2) &= \frac{\|\mathbf{s}_l\|^2 - \|\mathbf{s}_m\|^2}{r_l(k_i+2) + r_m(k_i+2)} \\ &- \frac{2(\mathbf{s}_l - \mathbf{s}_m)}{r_l(k_i+2) + r_m(k_i+2)} \left[\mathbf{p}(t_{k_i}) + 2T\mathbf{R}(t_{k_i})\mathbf{v}(t_{k_i})\right. \\ &\left. + 2T^2\mathbf{R}(t_{k_i})\mathbf{g}(t_{k_i}) + \mathbf{u}_1(k_i)\right] \\ &+ 2\frac{r_l(k_i+1) - r_m(k_i+1)}{r_l(k_i+2) + r_m(k_i+2)} b_c(t_{k_i}) \end{aligned}, \tag{26}$$

for all $l, m \in \{1, \ldots, L\}, l \neq m$. From the first L outputs of (14), for $k = k_i + 2$, using (20), (22), and (23) again, it is possible to write

$$\begin{aligned} r_l(k_i+2) - r_m(k_i+2) &= \frac{\|\mathbf{s}_l\|^2 - \|\mathbf{s}_m\|^2}{r_l(k_i+2) + r_m(k_i+2)} \\ &- \frac{2(\mathbf{s}_l - \mathbf{s}_m)}{r_l(k_i+2) + r_m(k_i+2)} \left[\mathbf{p}(t_{k_i}) + 2T\mathbf{R}(t_{k_i})\mathbf{x}_2(t_{k_i})\right. \\ &\left. + 2T^2\mathbf{R}(t_{k_i})\mathbf{x}_3(t_{k_i}) + \mathbf{u}_1(k_i)\right] \\ &+ 2\frac{r_l(k_i+1) - r_m(k_i+1)}{r_l(k_i+2) + r_m(k_i+2)} b_c(t_{k_i}) \end{aligned} \tag{27}$$

for all $l, m \in \{1, \ldots, L\}, l \neq m$. Taking the difference between (25) and (24), and the difference between (26) and (27), one can write, after simplification,

$$\begin{cases} 2[\mathbf{x}_2(k_i) - \mathbf{v}(t_{k_i})] + T[\mathbf{x}_3(k_i) - \mathbf{g}(t_{k_i})] = 0 \\ 2[\mathbf{x}_2(k_i) - 2\mathbf{v}(t_{k_i})] + 2T[\mathbf{x}_3(k_i) - \mathbf{g}(t_{k_i})] = 0 \end{cases} \tag{28}$$

for all $l, m \in \{1, \ldots, L\}, l \neq m$. Since the vectors $[2 \quad T]$ and $[2 \quad 2T]$ are linearly independent for $T \neq 0$, the solution of (28) is

$$\begin{cases} x_2(k_i) = \mathbf{v}(t_{k_i}) \\ x_3(k_i) = \mathbf{g}(t_{k_i}) \end{cases}. \tag{29}$$

The result in (29) concludes the proof of the theorem, since it has been shown that the initial condition of (9) corresponds to that of (14), in the conditions of the theorem. Since using Theorem 1 allows to conclude that the initial condition of (14) is uniquely determined and the two initial conditions from both systems match, it follows that the initial condition of (9) is also uniquely determined. □

4 Monte Carlo simulations

4.1 Setup

In order to evaluate the performance achieved by the proposed navigation algorithms, numerical simulations were performed. The vehicle described the trajectory shown in Fig. 2.

The initial position is $\mathbf{p}_0 = [150 \quad 150 \quad 70]^T(m)$, whereas the body-fixed velocity was assumed to be constant, with $\mathbf{v}(t) = [1 \quad 0 \quad 0]^T(m/s)$, and the bias that accounts for the effect of the clocks offset was set to $b_c(t) = 50\ m$. Even though the full nonlinear dynamics of the vehicle are not considered, the proposed filter still applies to any underwater vehicle since it relies solely on the vehicle kinematics, which are exact.

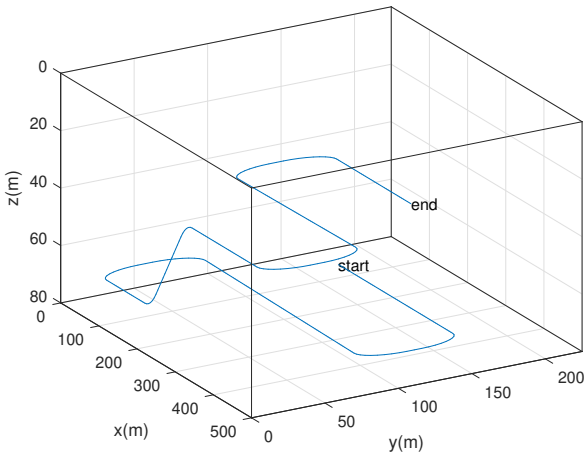

Fig. 2: Trajectory described by the underwater vehicle

The AHRS and IMU provide measurements with a frequency of 10 Hz, while the pseudo-range measurements have a sample time of 5 s. Sensor noise was considered in all sensors. The pseudo-ranges, acceleration and angular velocity are assumed to be corrupted by zero-mean white Gaussian noise, with standard deviations of 1 m, $2 \times 10^{-3}\ m/s^2$ and 0.05°/s, respectively. The attitude, which was parameterized by roll, pitch and yaw Euler angles, was assumed to be corrupted by zero-mean white Gaussian noise, with standard deviation of 0.03° for the roll and pitch and 0.3° for the yaw. The LBL configuration is composed of 5 beacons, with known positions, $\mathbf{s}_1 = [0 \quad 1000 \quad 0](m)$, $\mathbf{s}_2 = [0 \quad 1000 \quad 1000](m)$, $\mathbf{s}_3 = [1000 \quad 0 \quad 750](m)$, $\mathbf{s}_4 = [0 \quad 0 \quad 500](m)$, and $\mathbf{s}_5 = [250 \quad 0 \quad 250](m)$.

The state disturbance covariance matrix of the filter for the augmented system, i.e., a linear Kalman filter (LKF), was set to $\mathbf{Q} = \mathbf{diag}(10^{-3}\mathbf{I}, 10^{-4}\mathbf{I}, 10^{-5}\mathbf{I}, 10^{-1}, \mathbf{I})$, and the output noise covariance matrix was set to $\mathbf{R} = \mathbf{diag}(\mathbf{I}, 2\mathbf{I})$. In addition to the LKF, simulations with the extended Kalman filter and the unscented Kalman filter applied to the nonlinear system (9) were also carried out. The state disturbance covariance matrix of the extended Kalman filter (EKF) implementation to (9) was set to $\mathbf{Q} = \mathbf{diag}(10^{-3}\mathbf{I}, 10^{-4}\mathbf{I}, 10^{-5}\mathbf{I}, 10^{-1})$, and the output noise covariance matrix was set to $\mathbf{R} = \mathbf{I}$. The parameters for the unscented Kalman filter (UKF) are set to the optimal values for Gaussian distributions.

Subsequently, 1000 Monte Carlo simulation runs of 1200 seconds each were performed and the initial estimate $\mathbf{x}_0$ was set to the true value $\mathbf{x}_{0_{true}}$ with an added variable $\Delta\mathbf{x}$, which can be written as $\mathbf{x}_0 = \mathbf{x}_{0_{true}} + \Delta\mathbf{x}$, where $\Delta\mathbf{x}$ is a zero-mean Gaussian variable with standard deviation of $\sigma_p = 100\ m$ for the position, $\sigma_v = 0.2\ m/s$ for the velocity, $\sigma_g = 0.01\ m/s^2$ for the gravity acceleration, and $\sigma_{b_c} = 10\ m$ for the bias representing the clocks offset. The initial guess of the augmented states was obtained by the corresponding difference between the initial pseudo-ranges readings. The initial covariance $\mathbf{P}_0$ was set accordingly, written as $\mathbf{P}_0 = \mathbf{diag}\,[\sigma_p\mathbf{I}_3, \quad \sigma_v\mathbf{I}_3, \quad \sigma_g\mathbf{I}_3, \quad \sigma_{b_c}\mathbf{I}_3]$. The error is computed for each simulation and each sample. From these values, one extracts the mean-error and root-mean-square error (RMSE) for each sampled time, and the latter is compared to the Bayesian Cramér-Rao Bound (BCRB), which is detailed next.

4.2 Bayesian Cramér-Rao bound

The Bayesian Cramér-Rao Bound (BCRB) is a lower bound on the mean squared estimation error. Therefore, it is a useful reference to evaluate the performance of each algorithm. A recursive BCRB is derived in [28], for the case of a linear Gaussian process model and a nonlinear observation model with additive white Gaussian noise (AWGN). The recursion can be written as

$$\begin{aligned}\mathbf{J}(k+1) = &\left[\mathbf{Q} + \mathbf{F}(k)\mathbf{J}_n^{-1}\mathbf{F}(k)^T\right]^{-1} \\ &+ E_{\mathbf{x}(k+1)}\left\{\tilde{\mathbf{H}}^T(k+1)\mathbf{R}^{-1}\tilde{\mathbf{H}}(k+1)\right\},\end{aligned} \tag{30}$$

where $\mathbf{J}(k+1)$ is the BCRB, $\mathbf{Q}$ is the state disturbance intensity matrix which was already defined, $\mathbf{F}(k)$ is the state transition matrix, $\mathbf{H}(k)$ is a linear estimation of the observation model state matrix and $\mathbf{R}$ is the output noise intensity matrix, which was also already defined. The BCRB was calculated using the true state values $\mathbf{x}_{true}$ for each sampled time.

In order to illustrate the computed BCRB, its initial convergence and detailed evolution for the position are represented in Fig. 3.

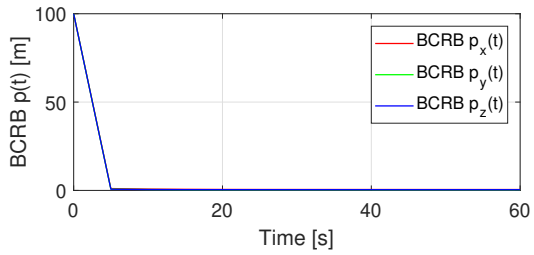

(a) Initial Convergence

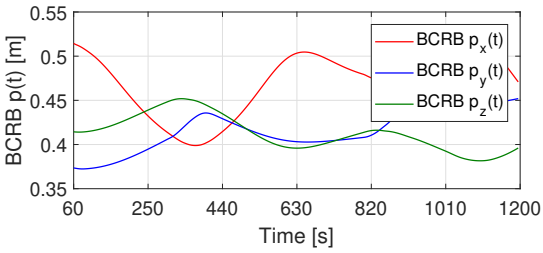

(b) Detailed evolution

Fig. 3: Initial convergence and detailed evolution of the Bayesian Cramér-Rao Bound for the position

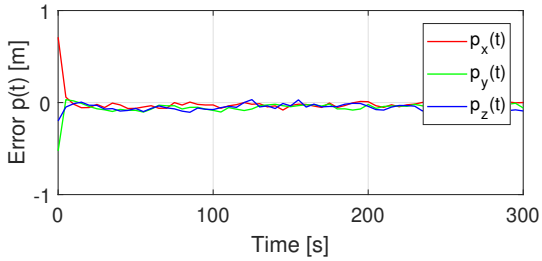

(a) LKF

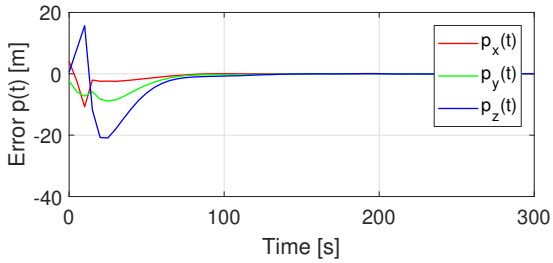

(b) EKF

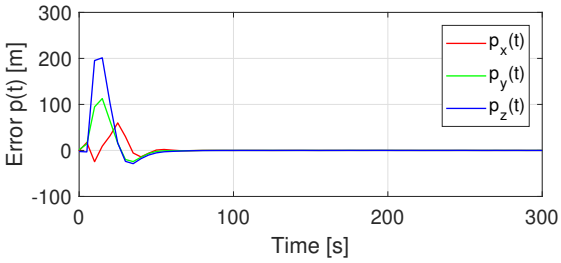

(c) UKF

Fig. 4: Initial convergence of the position mean-error

4.3 Initial convergence

The initial convergence of the position mean-error is presented in Fig. 4 for the LKF, EKF, and UKF. It can be concluded that the mean-error of the EKF and UKF, at 100 s, are close to zero, i.e., enter a stationary phase. The LKF however, presents a much faster convergence, with the position mean-error entering a stationary phase much sooner than the EKF and the UKF.

The initial convergence of the RMSE is portrayed in Fig. 5, for the LKF, EKF, and UKF. The convergence time is similar to the one for the mean-error. The LKF presents again the fastest convergence for the position RMSE. Similar conclusions can be drawn for the mean-error and RMSE of the velocity, gravity acceleration, and bias, which, for sake the of brevity, are omitted.

4.4 Detailed evolution

When considering the detailed evolution of the mean-error and RMSE, the different components of the position, velocity, and gravity acceleration evidence similar results. Thus, conclusions can be drawn from only one component of each, without loss of information.

The detailed evolution of the mean-error for the position $p_x(t)$, velocity $v_x(t)$, gravity acceleration $g_x(t)$, and bias $b_c(t)$ is presented in Figs. 6 to 9, respectively. Regarding the position mean-error, the LKF, EKF, and UKF have similar stationary phases, where each component of the position is usually below 0.1 m. The detailed evolution of the velocity and gravity acceleration mean-error shows bigger values for the UKF, which are typically below 0.02 m/s, and 2×10^{-3} m/s^2, respectively. The EKF, and LKF show similar results for these states, with mean-errors typically below 0.01 m/s for the velocity mean-error, and 5×10^{-4} m/s^2 for the gravity acceleration mean-error. The EKF maintains a zero-mean mean-error for the bias whereas the LKF and UKF do not, with the latter presenting the biggest mean-error.

The detailed evolution of the RMSE for the position $p_x(t)$, velocity $v_x(t)$, gravity acceleration $g_x(t)$, and bias $b_c(t)$ is presented in Figs. 10 to 13, respectively. The

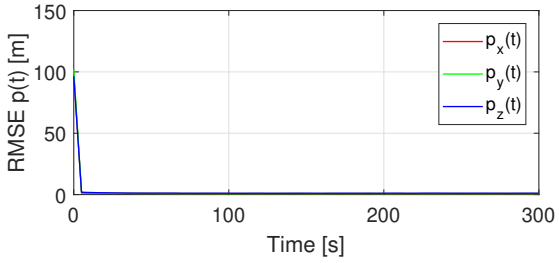

(a) LKF

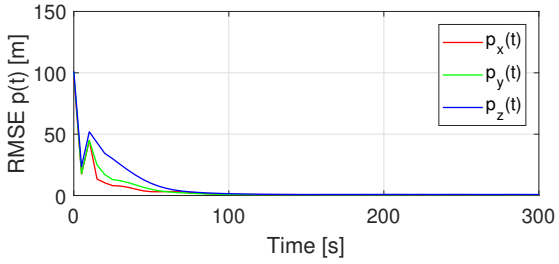

(b) EKF

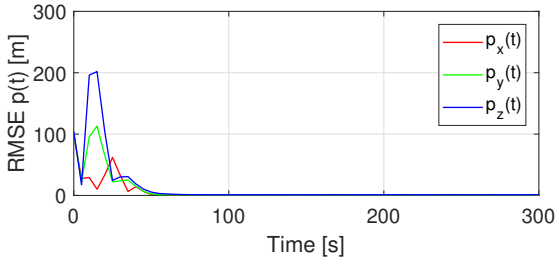

(c) UKF

Fig. 5: Initial convergence of the position RMSE

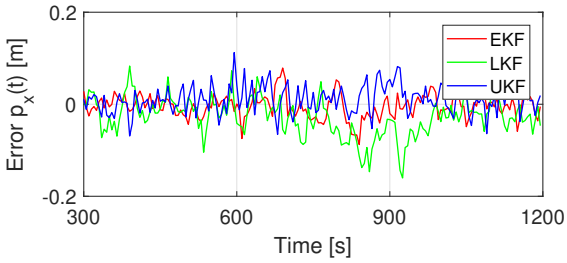

Fig. 6: Detailed evolution of the position $p_x(t)$ mean error

LKF and the EKF have a similar RMSE for every state, with the latter having slightly lower values. The RMSE of the UKF is typically bigger than the one obtained for the EKF and the LKF. This difference is specially noticeable on the computed RMSE for the velocity and acceleration of gravity. The BCRB effectively defines a lower bound for the RMSE.

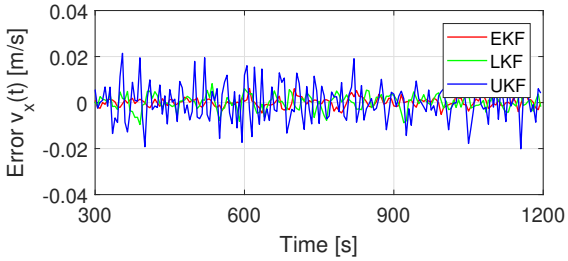

Fig. 7: Detailed evolution of the velocity $v_x(t)$ mean error

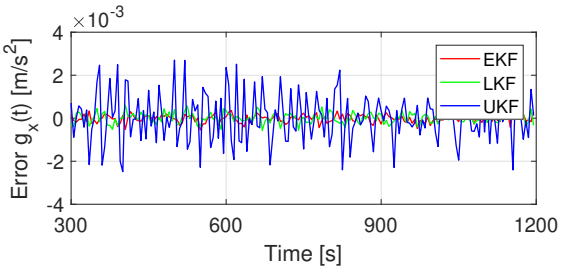

Fig. 8: Detailed evolution of the gravity acceleration $g_x(t)$ mean error

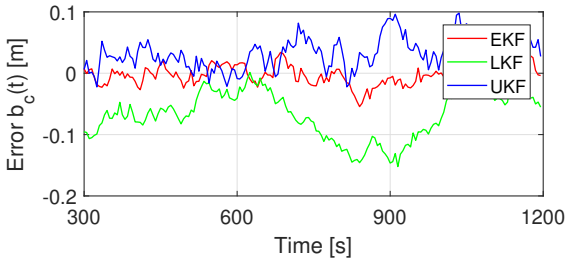

Fig. 9: Detailed evolution of the bias $b_c(t)$ mean error

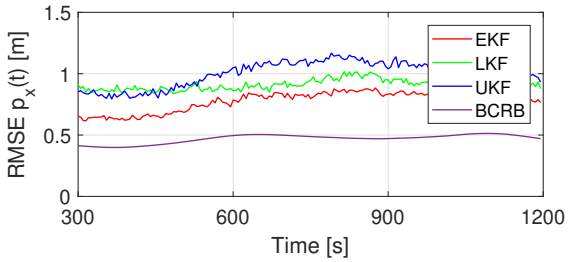

Fig. 10: Detailed evolution of the position $p_x(t)$ RMSE

4.5 Averages of the mean-error and RMSE

The averages of the mean-error and RMSE in steady-state are computed, and shown in Tables 2 to 5. As it is possible to conclude, the performance is compatible with usual navigation applications.

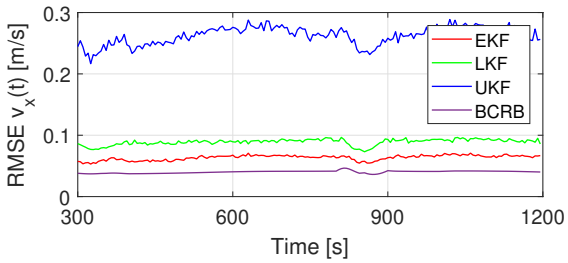

Fig. 11: Detailed evolution of the velocity $v_x(t)$ RMSE

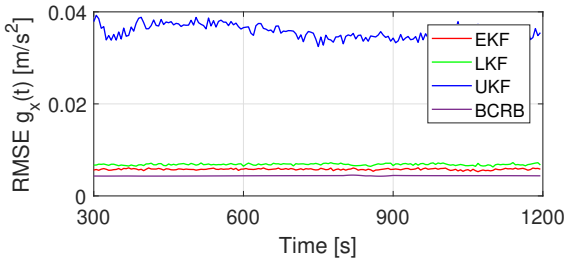

Fig. 12: Detailed evolution of the gravity acceleration $g_x(t)$ RMSE

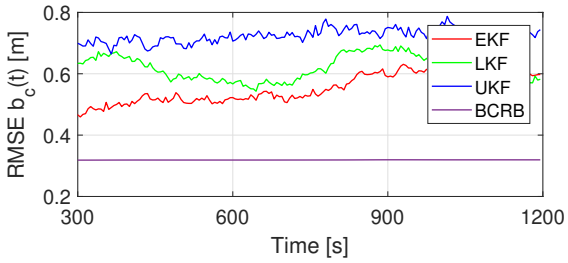

Fig. 13: Detailed evolution of the bias $b_c(t)$ RMSE

Table 2: Steady-state error for the x-component of the position, and velocity

Mean error	p_x (m)	v_x (m/s)
EKF	-8.9×10^{-2}	-1.0×10^{-5}
LKF	-2.4×10^{-2}	-4.5×10^{-5}
UKF	1.2×10^{-2}	9.4×10^{-5}

Table 3: Steady-state error for the x-component of the gravity acceleration, and the bias

Mean error	g_x (m/s^2)	**Bias** (m)
EKF	1.6×10^{-6}	2.2×10^{-2}
LKF	-6.1×10^{-6}	-5.8×10^{-2}
UKF	4.3×10^{-5}	3.1×10^{-2}

4.6 Processing time

The processing times are displayed in Table 6. The specifications for the computer used (laptop), are the following:

Table 4: Steady-state RMSE for the x-component of the position, and velocity

RMSE	p_x (m)	v_x (m/s)
EKF	7.8×10^{-1}	6.4×10^{-2}
LKF	9.0×10^{-1}	8.9×10^{-2}
UKF	1.0×10^{0}	2.6×10^{-1}

Table 5: Steady-state RMSE for the x-component of the gravity acceleration, and the bias

RMSE	g_x (m/s^2)	**Bias** (m)
EKF	5.8×10^{-3}	5.5×10^{-1}
LKF	6.8×10^{-3}	6.1×10^{-1}
UKF	3.6×10^{-2}	7.2×10^{-1}

- **Processor:** Intel (R) Core (TM) i7-7700HQ CPU @ 2.80GHz 2.80GHz
- **Graphics Card:** NVidia GeForce GTX 1050
- **RAM:** 16 GB DDR4-2400MHz
- **Disk:** SSD 512 GB
- **Operating System:** Windows 10 Home 64bit

From Table 6, it is possible to conclude that the LKF and the EKF have little difference in processing time, whereas the UKF is considerably more computationally expensive.

Table 6: Estimation time for each algorithm, for a single simulation and 1000 simulations

Time	**Single simulation**	**1000 simulations**
EKF	0.633 s	10 min 33 s
LKF	0.628 s	10 min 28 s
UKF	0.959 s	15 min 59 s

4.7 Filter non-convergence

To further illustrate the advantages of the LKF in regards to offering a global convergence guarantee, the condition of $\mathbf{x}_1(0) = [-3000 \quad -3000 \quad 1000]^T [m]$, $\mathbf{x}_2(0) = [100 \quad 100 \quad 100]^T [m/s]$, $\mathbf{x}_3(0) = [1000 \quad 1000 \quad 1000]^T [m/s^2]$, and $x_4(0) = -500\ m$ was chosen. The obtained results are presented in Figures 14, 15, and 16 for the position estimation of the EKF, UKF, and LKF, respectively. As it can be seen, both the EKF and the UKF fail to converge, whereas for the same initial condition, the proposed LKF converges.

5 Conclusions

This paper addresses the nonlinear problem of LBL navigation with pseudo-ranges and an IMU. The means

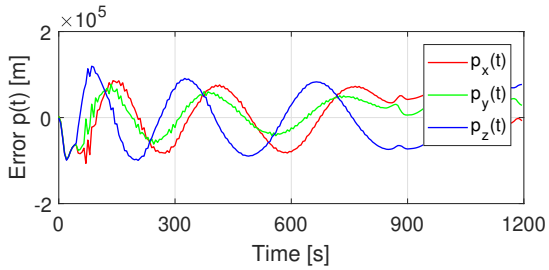

Fig. 14: Example of failure of the EKF

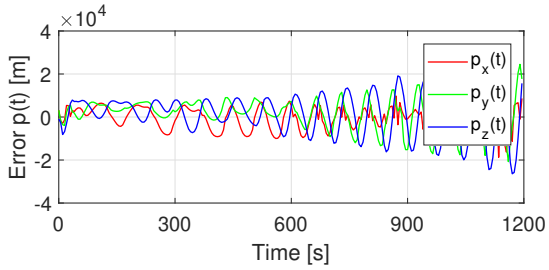

Fig. 15: Example of failure of the UKF

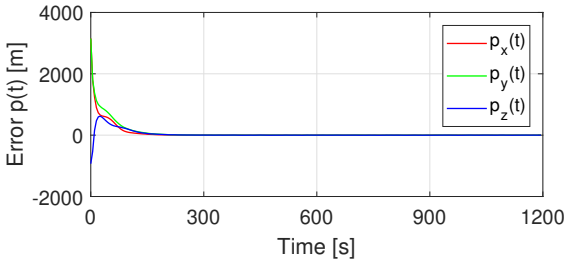

Fig. 16: Example of the LKF convergence for an initial condition which lead to failure of the EKF and UKF

to design an observer are provided with the derivation of a system that can be regarded as linear, to which a simple Kalman filter is applied. Globally exponentially stable error dynamics are established with the analysis of the observability of the system [12]. The devised solution successfully estimates the states of interest, and its performance was evaluated with simulations, including Monte Carlo runs. Both the mean-error and RMSE presented a smaller convergence time for the LKF, and similar stationary phases between the EKF, and LKF. The UKF showed the biggest mean-errors and RMSE, as well as the largest convergence time. An example of an initial condition with which the EKF and UKF do not converge, as opposed to the LKF, was shown, further illustrating the advantages of the latter regarding its guarantee of global convergence. In terms of computational cost, the UKF is substantially more demanding, whereas the LKF and the EKF are comparable. Taking all into account and considering that the EKF does not offer global convergence guarantees, one concludes that the novel LKF solution is the best among all three.

Compliance with Ethical Standards

Funding: This work was partially supported by the LARSyS - FCT Plurianual funding 2020-2023 and through the FCT project DECENTER [LISBOA-01-0145-FEDER-029605], funded by the Programa Operacional Regional de Lisboa 2020 and PIDDAC programs.

Conflict of interest: The authors declare that they have no further conflict of interest concerning the publication of this manuscript.

References

1. Batista, P.: GES Long Baseline Navigation with Clock Offset Estimation. In: European Control Conference (ECC), pp. 3011–3016. Strasbourg, France (2014)
2. Batista, P.: Long baseline navigation with clock offset estimation and discrete-time measurements. Control Engineering Practice **35**, 43–53 (2015). DOI 10.1016/j.conengprac.2014.10.009
3. Batista, P., Silvestre, C., Oliveira, P.: Position and velocity optimal sensor-based navigation filters for UAVs. In: Proceedings of the American Control Conference, pp. 5404–5409 (2009). DOI 10.1109/ACC.2009.5159877
4. Batista, P., Silvestre, C., Oliveira, P.: Sensor-based long baseline navigation: Observability analysis and filter design. Asian Journal of Control **16**(4), 974–994 (2014). DOI 10.1002/asjc.778
5. Bevly, D.M., Ryu, J., Gerdes, J.C.: Integrating INS sensors with GPS measurements for continuous estimation of vehicle sideslip, roll, and tire cornering stiffness. IEEE Transactions on Intelligent Transportation Systems **7**(4), 483–493 (2006). DOI 10.1109/TITS.2006.883110
6. Bobye, M., Fenton, P.: System and method for long baseline accelerometer/GNSS navigation (2016). URL https://patents.google.com/patent/US9933263B2/en. US Patent 9,933,263 B2
7. Brockett, R.: Finite Dimensional Linear Systems. Wiley (1970)
8. Chen, Y., Miller, P., Chen, Y., Miller, P.A., Farrell, J.A.: Underwater Inertial Navigation With Long Baseline Transceivers : A Near-Real-Time Approach Underwater Inertial Navigation with Long Base Line Transceivers : A Near-Real-Time Approach. IEEE Transactions on Control Systems Technology **24**(December), 240–251 (2013). DOI 10.1109/CDC.2013.6760680
9. Cheng, J., Yang, L., Li, Y., Zhang, W.: Seamless outdoor / indoor navigation with WIFI / GPS aided low cost Inertial Navigation System. Physical Communication **13**, 31–43 (2014). DOI 10.1016/j.phycom.2013.12.003. URL http://dx.doi.org/10.1016/j.phycom.2013.12.003
10. Diamant, R., Lampe, L.: Underwater localization with time-synchronization and propagation speed uncertainties. IEEE Transactions on Mobile Computing **12**(7), 1257–1269 (2013). DOI 10.1109/TMC.2012.100

11. Furfaro, T.C., Alves, J.: An application of distributed long baseline - Node ranging in an underwater network. 2014 Underwater Communications and Networking, UComms 2014 (2014). DOI 10.1109/UComms.2014.7017126
12. Jazwinski, A.H.: Stochastic processes and filtering theory. Dover Publication, Inc., Mineola, New York (1970). DOI https://doi.org/10.1016/S0076-5392(09)60372-6
13. Johannsson, H., Kaess, M., Englot, B., Hover, F., Leonard, J.: Imaging sonar-aided navigation for autonomous underwater harbor surveillance. IEEE/RSJ 2010 International Conference on Intelligent Robots and Systems, IROS 2010 - Conference Proceedings pp. 4396–4403 (2010). DOI 10.1109/IROS.2010.5650831
14. Jung, S.Y., Hann, S., Park, C.S.: TDOA-based optical wireless indoor localization using LED ceiling lamps. IEEE Transactions on Consumer Electronics **57**(4), 1592–1597 (2011). DOI 10.1109/TCE.2011.6131130
15. Kebkal, K.G., Kebkal, O.G., Kebkal, V.K., Petroccia, R.: Synchronization tools of acoustic communication devices in control of underwater sensors, distributed antennas, and autonomous underwater vehicles. Gyroscopy and Navigation **5**(4), 257–265 (2014). DOI 10.1134/S2075108714040063
16. Kelly, A.: Modern Inertial and Satellite Navigation Systems (1994)
17. Mariani, S., Ghisi, A.: Unscented Kalman filtering for nonlinear structural dynamics. Nonlinear Dynamics **49**(1-2), 131–150 (2007). DOI 10.1007/s11071-006-9118-9
18. Milne, P.H.: Underwater Acoustic Positioning Systems. Gulf Publishing Company (1983)
19. Moore, J.B., Qi, H.: Direct Kalman Filtering Approach for GPS/INS Integration[A]. IEEE Transactions on Aerospace and Electronic Systems[C] **38**(2), 687–693 (2002)
20. Paull, L., Saeedi, S., Seto, M., Li, H.: AUV navigation and localization: A review. IEEE Journal of Oceanic Engineering **39**(1), 131–149 (2014). DOI 10.1109/JOE.2013.2278891
21. Rigby, P., Pizarro, O., Williams, S.: Towards Geo-Referenced AUV Navigation Through Fusion of USBL and DVL Measurements. In: Oceans 2006, 2. IEEE, Boston, USA (2006). DOI 10.1109/OCEANS.2006.306898
22. Shabani, M., Gholami, A., Davari, N.: Asynchronous direct Kalman filtering approach for underwater integrated navigation system. Nonlinear Dynamics **80**(1-2), 71–85 (2015). DOI 10.1007/s11071-014-1852-9
23. Shen, S.C., Chen, C.J., Huang, H.J., Pan, C.: Evaluation of MEMS inertial sensor module for underwater vehicle navigation application. 2010 International Conference on Mechanic Automation and Control Engineering pp. 3807–3810 (2010). DOI 10.1109/MACE.2010.5535510
24. Silva, T., Batista, P.: GES INS-aided Long Baseline Navigation with clock offset estimation and discrete-time measurements. Proceedings of the 2019 European Control Conference (2019)
25. Skog, I., Peter, H.: Time synchronization errors in GPS-aided inertial navigation systems. Ieee Transactions on Intelligent Transportation Systems **X**(X), 1–15 (2008)
26. Sukkarieh, S., Nebot, E.M., Durrant-Whyte, H.F., Others: A high integrity IMU GPS navigation loop for autonomous land vehicles applications. IEEE Trans. on Robotics & Automation **15**(3), 572–578 (1999)
27. Techy, L., Morganseny, K.a., Woolseyz, C.a.: Long-baseline acoustic localization of the Seaglider underwater glider. Proceedings of the 2011 American Control Conference pp. 3990–3995 (2011). DOI 10.1109/ACC.2011.5991416
28. Trees H., B.K.: Bayesian Bounds for Parameter Estimation and Nonlinear Filtering/Tracking. Wiley (2007)
29. Vermeij, A., Munafo, A.: A Robust, Opportunistic Clock Synchronization Algorithm for Ad Hoc Underwater Acoustic Networks. IEEE Journal of Oceanic Engineering **40**(4), 841–852 (2015). DOI 10.1109/JOE.2015.2469955
30. Woodman, O.J.: An introduction to inertial navigation. Tech. Rep. 696, University of Cambridge (2007)
31. Zhang, J., Han, Y., Zheng, C., Sun, D.: Underwater target localization using long baseline positioning system. Applied Acoustics **111**, 129–134 (2016). DOI 10.1016/j.apacoust.2016.04.009. URL http://dx.doi.org/10.1016/j.apacoust.2016.04.009
32. Zhang, W., Kavehrad, M.: A 2-D indoor localization system based on visible light LED. 2012 IEEE Photonics Society Summer Topical Meeting Series, PSST 2012 **4**, 80–81 (2012). DOI 10.1109/PHOSST.2012.6280711